Flow Fields Control Nanostructural Organization in Semiflexible Networks

Supplemental information

Tomas Rosén,[*,†,‡,¶] Nitesh Mittal,[†,‡,§] Stephan V. Roth,[‖,⊥] Peng Zhang,[‖,#]

Fredrik Lundell,[†,‡] and L. Daniel Söderberg[†,‡]

†*Wallenberg Wood Science Center, Royal Institute of Technology, SE-100 44 Stockholm, Sweden*

‡*Linné FLOW Center, KTH Mechanics, Qsquars backe 18, Royal Institute of Technology, SE-100 44 Stockholm, Sweden*

¶*Present address: Treesearch, KTH Royal Institute of Technology, Teknikringen 56-58, SE-100 44 Stockholm, Sweden*

§*Present address: Department of Chemical Engineering, Massachusetts Institute of Technology, 77 Massachusetts Avenue, Cambridge, MA 02139, USA*

‖*DESY, Notkestrasse 85, Hamburg, Germany*

⊥*Department of Fibre and Polymer Technology, Teknikringen 56-58, Royal Institute of Technology, SE-100 44 Stockholm, Sweden*

#*Present address: School of Materials Science and Engineering, PCFM Lab, Sun Yat-sen University, Guangzhou, 510275, China*
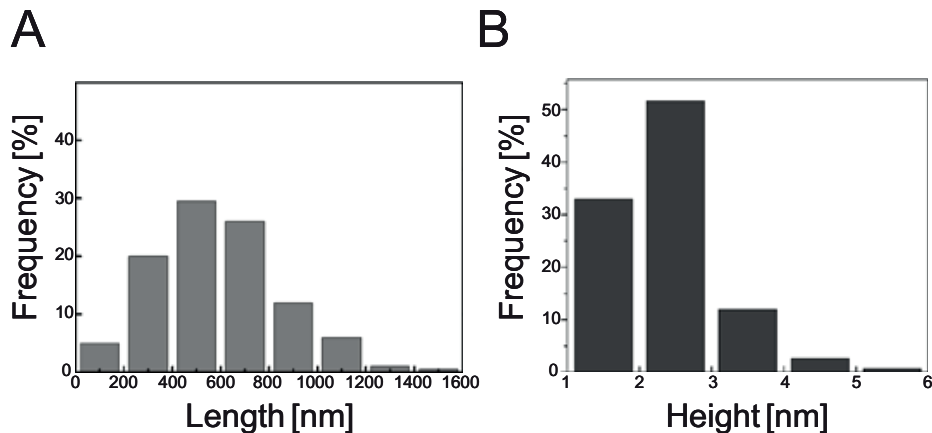
E-mail: trosen@kth.se

Figure 1: Characterization of CNF fibril dimensions. Distribution of length measured with TEM (a) and height measured with AFM (b); data has been obtained from Mittal et al.[1] with permission.
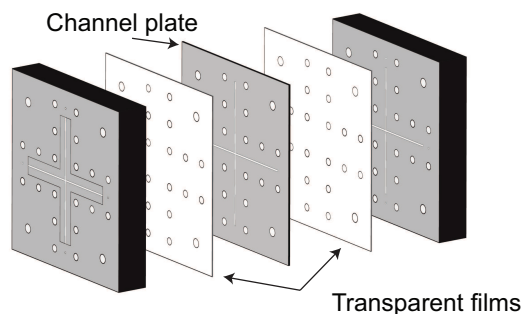

Figure 2: Illustration of the assembly of the experimental flow cell; a channel plate is sandwiched between two transparent films; aluminum plates are placed outside for mechanical support.

Length and width distribution of nanofiber suspensions

The CNF length and width distributions obtained with TEM and AFM, respectively, are illustrated in Fig. 1. The procedure is described in the main text.

Flow cell assembly

The flow cell is illustrated in Fig. 2 and consists of a channel plate, two polymer films used as window material (either Kapton for SAXS experiments or COC for POM experiments)
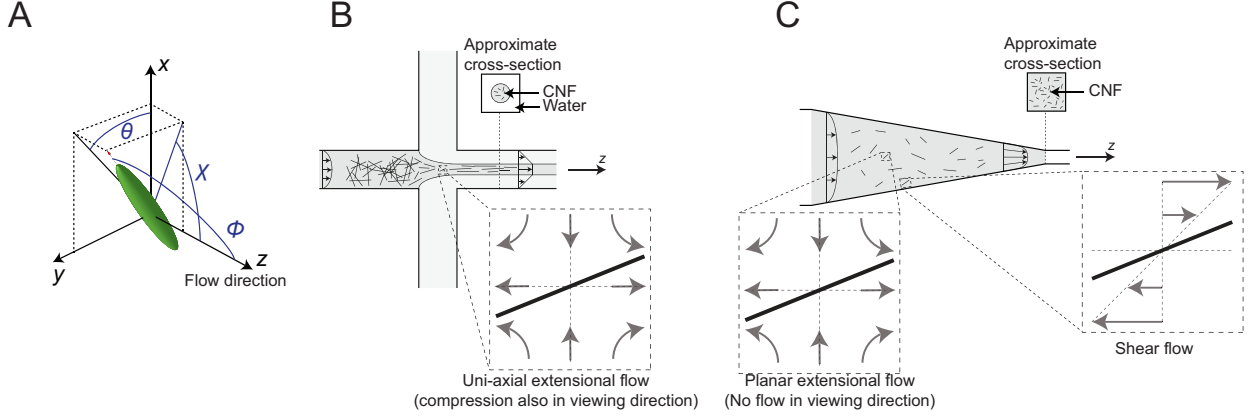
Figure 3: (a) Orientation of an elongated particle described by the polar angle ϕ and the azimuthal angle θ with respect to flow direction z; the projected angle observed in the xz-plane is denoted χ; Illustration of the different velocity gradients that the CNF dispersion is experiencing in the two channel geometries; (b) the particles on the centerline in the flow-focusing channel geometry (FFC) are experiencing a uni-axial extensional flow; (c) the particles on the centerline in the converging channel geometry (CC) are experiencing a planar extensional flow while particles close to the walls are experiencing shear flow.

and two 10 mm aluminum plates that are mounted together using screws.

Two channel geometries were used in the study as described in the main text: a flow-focusing channel (FFC) geometry and a converging channel (CC) geometry. The characteristic length scale throughout this work is used as $h = 1$ mm. The geometries are illustrated in Fig. 1 in the main manuscript.

The FFC geometry has a cross shape with four perpendicular channels, each with a square cross section of $h \times h$, where three serves as inlets and one as outlet. A core flow of the cellulose nanofibril (CNF) dispersion (flow rate Q_1) is focused by two perpendicular sheath flows of water (each with flow rate Q_2).

The CC geometry has initially a rectangular cross-section of $4h \times h$, which is linearly contracted to $h \times h$ over a length of $10h$.

Difference between channel geometries

The general flow direction in the experiment is defined to be the z-direction. To describe the orientation of a single fibril, we will use the polar angle ϕ as the angle between the fibril major axis and the flow (z) direction while the azimuthal angle θ is the projected angle in the plane perpendicular to the flow (see Fig. 3). The projected angle in the plane perpendicular to the viewing direction is denoted χ. The probability of a single fibril having a certain orientation ϕ and θ is given by the orientation distribution functions (ODF) Ψ_ϕ and Ψ_θ, respectively. To describe the average alignment of the CNF in the flow direction, the order parameter $S_\phi = \frac{1}{2}\langle 3\cos^2\phi - 1 \rangle$ is used. The brackets in this expression denote an ensemble average over all fibrils.

In both channel geometries, the CNF dispersion is accelerated, leading to an increased alignment of the fibrils. There are however some key differences between the FFC and CC geometries that are illustrated in Fig. 3b and c.

Firstly, when changing the acceleration in the FFC geometry by changing Q_1 and Q_2, the cross-section of the core will also change. Using SAXS or POM to characterize the alignment will therefore result in difficulties in comparing the effect of increasing acceleration since there will also be less amount of CNF in a channel cross-section. Furthermore, at high accelerations the core flow might fluctuate spatially due to instabilities of the flow, while low accelerations can cause a transition to a flow regime where the core fluid is not detached from the walls.[2] In the CC geometry on the other hand, the acceleration can be increased with Q without changing the amount of CNF in the channel cross-section. Furthermore, the flow is also more stable at high accelerations.

Secondly, in the FFC geometry, the fibrils in the core are approximately only experiencing a uni-axial extensional flow.[3] An assumption can thus be made about cylindrical symmetry around the centerline, with a uniform distribution of the angle θ ($\Psi_\theta = $ constant). Furthermore, Ψ_ϕ can be assumed not to vary over the core cross-section. In this channel it is thus possible to easily obtain the steady state ODF $\Psi_{\phi,0}$ from SAXS experiments using the recon-
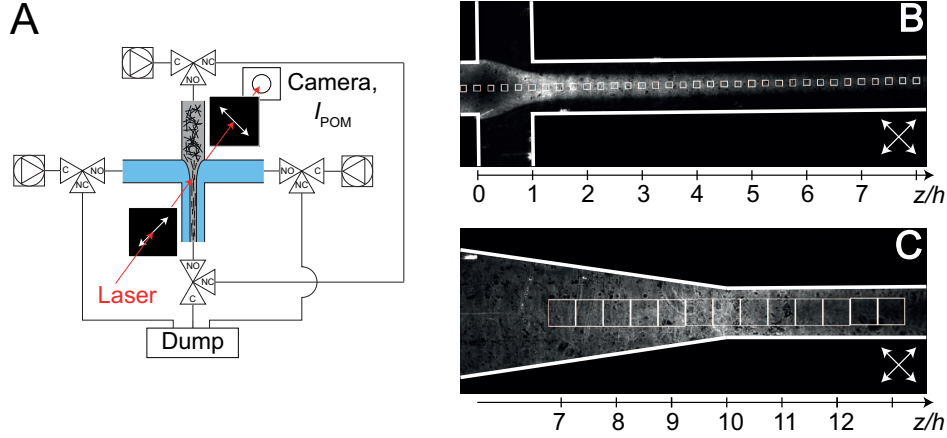
Figure 4: Illustration of the POM experiment; (a) Schematic illustration of the POM flow-stop experiment; (b) example POM image during stationary flow in the FFC geometry; (c) example POM image during stationary flow in the CC geometry; white squares indicate the downstream measurement locations.

struction method by Rosén et al.[4]. In the CC geometry, close to the walls, the particles are experiencing velocity gradients in the wall normal directions, i.e. a shear flow in addition to the extensional flow due to the acceleration. The rotational motion of elongated particles in shear differs from that in extension; in shear, the particles are performing a flipping motion in contrast to the pure aligning occurring in extensional flow.[5] The orientation distribution in the CC channel can thus not be assumed to be constant over the channel cross-section, as there are differences in extension/shear levels depending on the distance from the walls.

POM flow-stop experiments

Experimental setup and Measurement locations

The flow cell is placed between two cross-polarized linear polarization filters, with angles $+45°$ and $-45°$ with respect to the flow direction according to Fig. 4a. A wide laser module illuminates uniformly a circular spot of approximately 10 mm in diameter. The transmitted laser light intensity through filters and flow cell is recorded on a camera. The flow is distributed with syringe pumps and the flow can be stopped by instantly redirecting the flow

with synchronized three-way valves. At stop, the Common port (C) is instantly disconnected from the Normally Open (NO) port and connected with the Normally Closed (NC) port (see Fig. 4a).

The experimental flow cell is placed such that 1 mm corresponds to approximately 66 pixels on the camera image. For evaluating the POM intensity at a certain downstream location z, a region of interest (ROI) is selected in the image, where the average pixel intensity is used for analysis.

In the flow-focusing channel (FFC) geometry, the ROIs are illustrated in Fig. 4b. The center point of each ROI is placed at $z/h = -0.25, 0, 0.25, \ldots, 8$ and the side of each square ROI is approximately 0.125 mm, leading to the intensity average taken over $\approx$ 60-70 pixels.

In the converging channel (CC) geometry, the ROIs are illustrated in Fig. 4c. The center point of each ROI is placed at $z/h = 7, 7.5, \ldots, 13$ and the side of each square ROI is approximately 0.5 mm, leading to the intensity average taken over $\approx$ 1000 pixels.

POM Theory

The light illuminating the channel in the POM experiments can be decomposed into light polarized parallel and perpendicular to the z-direction. As the fibrils align in the z-direction, they also affect the birefringence of the dispersion. This means that light polarized in the z-direction will experience a different refractive index $n_\parallel$ when traveling through the dispersion than the refractive index $n_\perp$ for light with perpendicular polarization. The difference in refractive indices $\Delta n = n_\parallel - n_\perp$ causes a phase shift $\Delta\varphi$ between the two components. This phase shift can be measured by placing linear polarization filters on each side of the birefringent sample. These have polarization directions $45°$ and $-45°$ to the z-direction, respectively. The transmitted light intensity I_{POM} through the filters and the sample is related to Δn through the approximation:[6]

$$I_{\mathrm{POM}} \approx I_0 \left(\frac{2\pi d}{\lambda}\right)^2 (\Delta n)^2, \tag{1}$$

where d is the distance that the light has traveled through the sample, λ is the wavelength of the light and I_0 is the intensity of the incoming light. This expression holds as long as $I_{\text{POM}} \ll I_0$ and the angle that the sample has rotated the light is much less than $90°$, which is assumed to be the case in the present experiments. Furthermore, the difference in refractive indices Δn is related to the order parameter S_ϕ through:[7]

$$S_\phi = \frac{\Delta n}{\Delta n_{\text{max}}}, \tag{2}$$

where Δn_{max} corresponds to the difference in refractive index at perfect alignment ($S_\phi = 1$). The order parameter can consequently be found in POM experiments using:

$$S_\phi = S_{\phi,\text{ref}} \sqrt{\frac{I_{\text{POM}}}{I_{\text{POM,ref}}}}, \tag{3}$$

given that an absolute value of the order parameter $S_{\phi,\text{ref}}$ and the corresponding light intensity $I_{\text{POM,ref}}$ are known for a certain reference case. Without these reference values, only relative measurements of the order parameter can be obtained. At the same time, it is known that the order parameter of a dilute dispersion only subject to Brownian diffusion decays as[8–10]

$$S_\phi(z,t) = S_{\phi,0}(z) \exp(-6D_r t). \tag{4}$$

Rotary diffusion coefficients can thus be obtained through the decay of the intensity signal $I_{\text{POM}}(t)$ by combining equations 4 and 3 and using the stationary order parameter at position z as reference case:

$$I_{\text{POM}}(z,t) = I_{\text{POM},0}(z)e^{-12D_r t}. \tag{5}$$

In order to only observe the influence of the light from the CNF, a background subtraction is done using measurements with water flowing through the channel. We also divide the subtracted intensity with the same background intensity, to remove any effects of the laser light not being completely uniform over the field of view, i.e.

$$I_{\text{POM,raw}}(z,t) = \frac{I_{\text{POM,CNF}}(z,t) - I_{\text{POM,background}}(z)}{I_{\text{POM,background}}(z)}, \tag{6}$$

where the intensity recorded on the 8-bit camera is ranging between 0 and 255. The intensity $I_{\text{POM,raw}}$ in this case however does not decay to zero, as the optical properties of the equilibrium state of the CNF dispersion seems to be different from water. As this equilibrium level $I_{\text{eq.}} = I_{\text{POM,raw}}(z, t \to \infty)$ is not consistently positive or negative (after the background subtraction), we can not draw any conclusions about its origin. Therefore, the mean intensity during the last second of the experiment (around 9 s after stop) is set as the equilibrium level $I_{\text{eq.}}$ and the true intensity is given by $I_{\text{POM}} = I_{\text{POM,raw}} - I_{\text{eq.}}$. A zero-level is further introduced at $I_{\text{POM}} = 10^{-2}$, below which no analysis of intensity is done.

Each POM flow-stop experiment is initialized by starting the syringe pumps. After approximately 5 s of flow, the camera is recording 1500 frames with a rate of 100 frames per second. After approximately 5 s of recording the valves are switched to stop the flow in the flow cell, and the remaining time of approximately 10 s is recorded to measure the decay of birefringence.

The steady state intensity during flow $I_{\text{POM},0}(z)$ is taken as the mean intensity in a two second period just before the flow is stopped. The exact stopping time is found manually as the first frame unaffected by the stop.
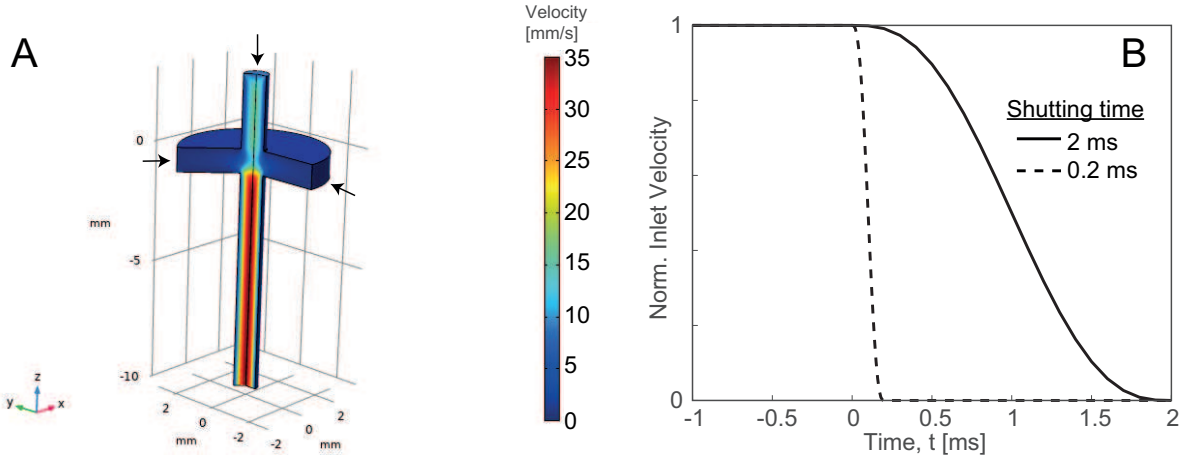
8

Figure 5: Illustration of the Comsol simulations used to assess the inertial effects during stop; (a) the flow is analyzed in a simplified geometry with cylindrical symmetry with same volumetric flow rates as in the experiments (core flow 23.4 ml/h and sheath flow 27 ml/h); (b) the stopping of the flow is realized by implementing a gradually decreasing inlet velocity with two shutting times: 2 ms (solid curve) and 0.2 ms (dashed curve).

All images from the flow-stop experiment in the main manuscript to display steady state POM intensity and relaxation rates after stop, averaged over repeated experiments, are median-filtered only for illustrative purposes, and not for analysis.

Assessment of inertial effects during stop

The flow will never be stopped instantly due to fluid inertia, and there will always be a relaxation process where the flow is adapting to the new boundary conditions with possible velocity gradients appearing during the initial few milliseconds after stop. To assess this potential issue, numerical simulations were performed using Comsol Multiphysics v5.5 of a flow-focusing system with cylindrical symmetry (see Fig. 5a). The flow is initially set up with the same core and sheath volumetric flow rates as in the experiment. The shutting sequence of the valve was modeled using a smoothed Heaviside function at the inlets with two different shutting times of $t_{\text{valves}} = 2$ ms and 0.2 ms (Fig. 5b). The flow was then studied during the period until it comes to a complete stop. Both core and sheath fluids were modeled as water (at room temperature), which in terms of inertial effects would be a worst-case scenario, as
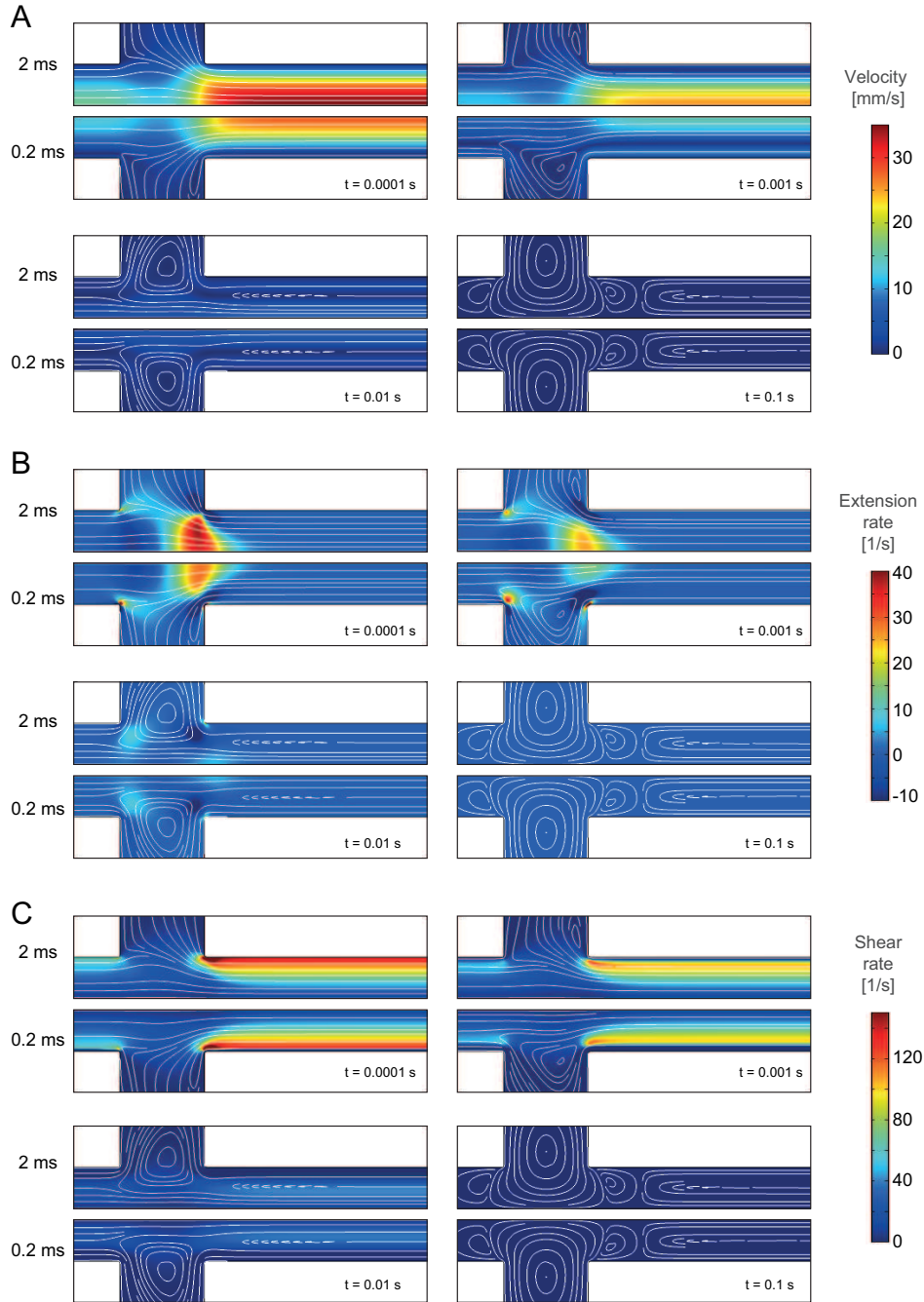
Figure 6: Flow profiles during four time instances ($t = 0.1, 1, 10$ and 100 ms) of the stopping sequence; (a) total velocity magnitude; (b) extension rate (dw/dz) and (c) shear rate (dw/dr); upper and lower images show the flow field for shutting times 2 ms and 0.2 ms, respectively.
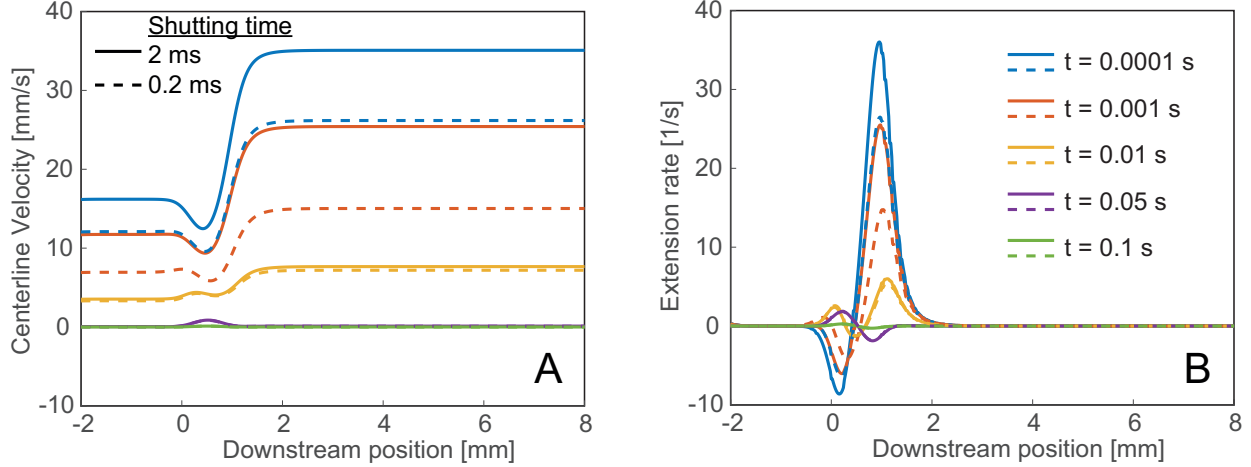
Figure 7: Centerline data during five time instances ($t = 0.1, 1, 10, 50$ and 100 ms) of the stopping sequence; (a) centerline velocity w; (b) extension rate dw/dz.

the CNF dispersion typically has 100-1000 times higher viscosity.

Fig. 6a shows the streamlines and total velocity rate in the channel for both shutting times at four different time instances after stop: 0.1 ms, 1 ms, 10 ms and 100 ms. Similarly the extension rate (dw/dz) and shear rate (dw/dr) is illustrated the same way in Fig. 5b and c. The centerline velocity and extension rate are plotted versus downstream position in Fig. 7.

The streamlines show that there are some possible re-circulation regions appearing in the sheath flow channel. However, since the fluid velocity in these regions is vanishingly small, there is basically no back-flow at any time during stop. Overall, the general tendency is that the velocity just gradually decreases to zero. Interestingly, the shutting time only influences the flow over the first 1 ms, while at 10 ms, the flow fields are in principle identical. In conclusion, the time to reach a complete stop is of the order of $t_{\text{stop}} = 50$ ms and is independent of the shutting time (as long as $t_{\text{valves}} < 50$ ms), but of course dependent on inertia in the flow. With less inertia in the flow, t_{stop} will approach t_{valves}.

There is however an effect worth noting with respect to the extension rate on the centerline (Fig. 7b). For rotational dynamics of particles, this is also more relevant than the absolute velocity. At around 50 ms, there is clearly an overshoot of the velocity gradients

11

causing them to change sign on the centerline, which could potentially affect CNF alignment as the flow is slightly compressed. However, the total deformation is so small since it is only present approximately during 50 ms. With more inertia in the flow, this overshooting extension rate and total deformation might potentially being large enough to affect the CNF de-alignment during the stopping sequence. This sets a practical limit also to what flow rates that can be used for this type of experiment.

From the experiment, recording at a frame rate of 100 fps, any effect below 10 ms can not be observed. It is clear however that since alignment is still high after 10 ms, it can be concluded that any inertial effects from the stopping will not affect the de-alignment of the nanofibrils. Furthermore, by tracking impurities in the flow, it can be concluded that the flow is completely stopped within pixel resolution. The typical stopping time of the slider-valves in the experiment is of the order of $t_{\mathrm{valves}} = 10$ ms (derived from the switching time provided by manufacturer). Due to the much higher viscosity of the CNF dispersion, we can neglect the inertial effect and estimate the time for the flow to reach a complete stop to be of the same order as the provided stopping time, i.e. $t_{\mathrm{stop}} \approx 10$ ms.

For the experiments in the converging channel, since there is only CNF dispersion present in the channel, fluid inertial effects are estimated to be even smaller owing to the high viscosity compared to water, even though flow rates are up to 4 times larger.

SAXS experiments

Experimental setup

A photograph of the experimental setup at the P03 Beamline (PETRA III, DESY, Hamburg) is shown in Fig. 8a. The flow cell is placed on a traversing stage with the fluids being driven by remote controlled syringe pumps. The X-ray beam is transmitted through the flow cell and the scattered photons are collected on a detector at a distance of $D = 7.5$ m from the flow cell (see Fig. 8b). An example of an averaged scattering image after background

subtraction at position $z = 2h$ in the FFC geometry is illustrated in Fig. 8c. Note that the horizontal and vertical lines represent intermodule gaps on the detector and the other blue areas correspond to detector pixels that are shadowed by beamstops and flight tube. None of these pixels contain any scattering information and are not used in the SAXS analysis. The azimuthal anisotropy of the scattering intensity around the center of the beam represents the alignment of the CNF in the channel. The SAXS experiments where only performed on the FFC geometry.

Theory

As an X-ray beam is passing through the dispersion of CNF, the fluctuations of the electron distribution (due to the solid particles) gives rise to scattered light.[11] The scattered light intensity contains structural information of the particles and can therefore also be used to quantify the alignment of the CNF. The present procedure to analyze the SAXS data is similar to Håkansson et al.[3] and the additional considerations to obtain S_ϕ is described in detail by Rosén et al.[4].

The scattered light intensity is probed for different scattering vectors $\boldsymbol{q}$ with direction given by:[11]

$$\boldsymbol{e_q} = \frac{\boldsymbol{e}_{\text{scat.}} - \boldsymbol{e}_{\text{inc.}}}{|\boldsymbol{e}_{\text{scat.}} - \boldsymbol{e}_{\text{inc.}}|}, \tag{7}$$

where $\boldsymbol{e}_{\text{scat.}}$ and $\boldsymbol{e}_{\text{inc.}}$ refer to unit vectors of the scattered and incident light, respectively. The length of the scattering vector is given by:[11]

$$|\boldsymbol{q}| = \frac{4\pi}{\lambda} \sin \varphi, \tag{8}$$

where λ is the wavelength of the X-ray and 2φ is the angle between $\boldsymbol{e}_{\text{scat.}}$ and $\boldsymbol{e}_{\text{inc.}}$. In small

angle scattering experiments, the assumption $\sin \varphi \approx \varphi$ holds and we can probe the scattering intensity on a flat detector, where pixel coordinates x_d and z_d corresponds to scattering vector components:[11]

$$q_x = \frac{2\pi x_d}{\lambda D}, \qquad q_z = \frac{2\pi z_d}{\lambda D}, \qquad (9)$$

for the sample-to-detector distance D. To remove any contribution from the solvent, a background subtraction was done with scattering from pure water in the channel. An example of a scattering intensity image is showed in Fig. 9a. The dead pixels on the detector and pixels behind the beamstop were first needed to be corrected. This was done by using the fact that the scattering pattern is symmetric and should ideally contain the same information at $(\pm q_x, \pm q_z)$. A pixel without information in the image was thus corrected by replacing its value by a value from any of the other three "mirror" pixels. The resulting intensity image after this procedure is illustrated in Fig. 9b. The pixel coordinates are transformed to the cylindrical coordinates $q = \sqrt{q_x^2 + q_z^2}$ and $\chi = \tan^{-1}(q_x/q_z)$. We then construct a histogram of $I_{\text{SAXS}}(q, \chi)$ in the range $q \in [0.25, 0.5]$ nm^{-1} (Fig. 9c) with certain number of bins in q- and χ-directions. The number of bins in q- and χ-direction was chosen to be significantly lower than the number of pixels in the q- and χ-directions, respectively. This is ensuring that each histogram bin contains information.

For each subrange of q, the isotropic contribution to the scattering is removed by assuming that the highest aligned case (at $z = 1.5h$) has no fibers aligned perpendicular to the flow. This means that all intensity values in the q-subrange are subtracted by $I_{iso}(q) \approx I_{\text{SAXS}}(q, \chi = \pm \pi/2)$. It should be mentioned that the isotropic contribution I_{iso} amounts to a majority of the total scattering intensity, which might indicate that a majority of nanofibrils actually are not aligned. Each subrange in q is then normalized, the subranges are averaged and we obtain the steady state orientation distribution function (ODF) of $\Psi_{\chi,0}$ (Fig. 9d). The measurement thus gives the average projected angle χ of particles in the

viewing (xz) plane, as illustrated in Fig. 3a. This angle is related to ϕ and θ through the relationship:

$$\tan \chi = \tan \phi \cos \theta. \tag{10}$$

To obtain the ODF of the polar angle ϕ, we make the assumption that the azimuthal angle θ is distributed uniformly in the flow. The steady state ODF $\Psi_{\phi,0}$ is then obtained with the same method as described by Rosén et al.[4]. The corresponding steady state order parameter $S_{\phi,0}$ is found through:

$$S_{\phi,0} = \int_{-\pi/2}^{\pi/2} \Psi_{\phi,0} \left(\frac{3}{2} \cos^2 \phi - \frac{1}{2} \right) |\sin \phi| d\phi. \tag{11}$$

with normalization

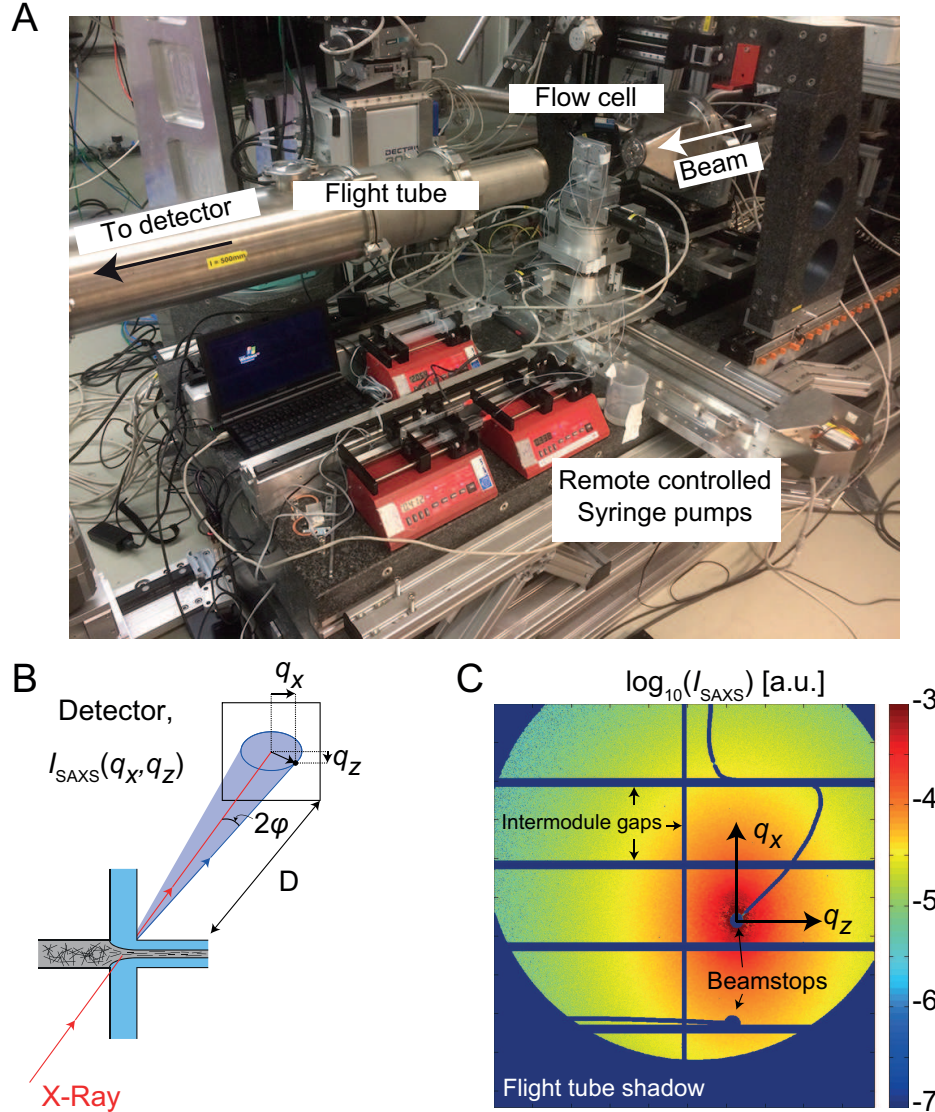$$\int_{-\pi/2}^{\pi/2} \Psi_{\phi} |\sin \phi| d\phi = 1. \tag{12}$$

Figure 8: Illustration of the SAXS experiment; (a) the actual experimental setup at the P03 Beamline, PETRA III, DESY, Hamburg; (b) schematic illustration of the experimental setup; (c) example detector image from the SAXS experiment taken in the FFC geometry at $z = 2h$; pixels at the intermodule gaps on the detector as well as pixels shadowed by the flight tube and beamstops contain no data and are not used in the SAXS analysis; note that the lower beamstop has no role.
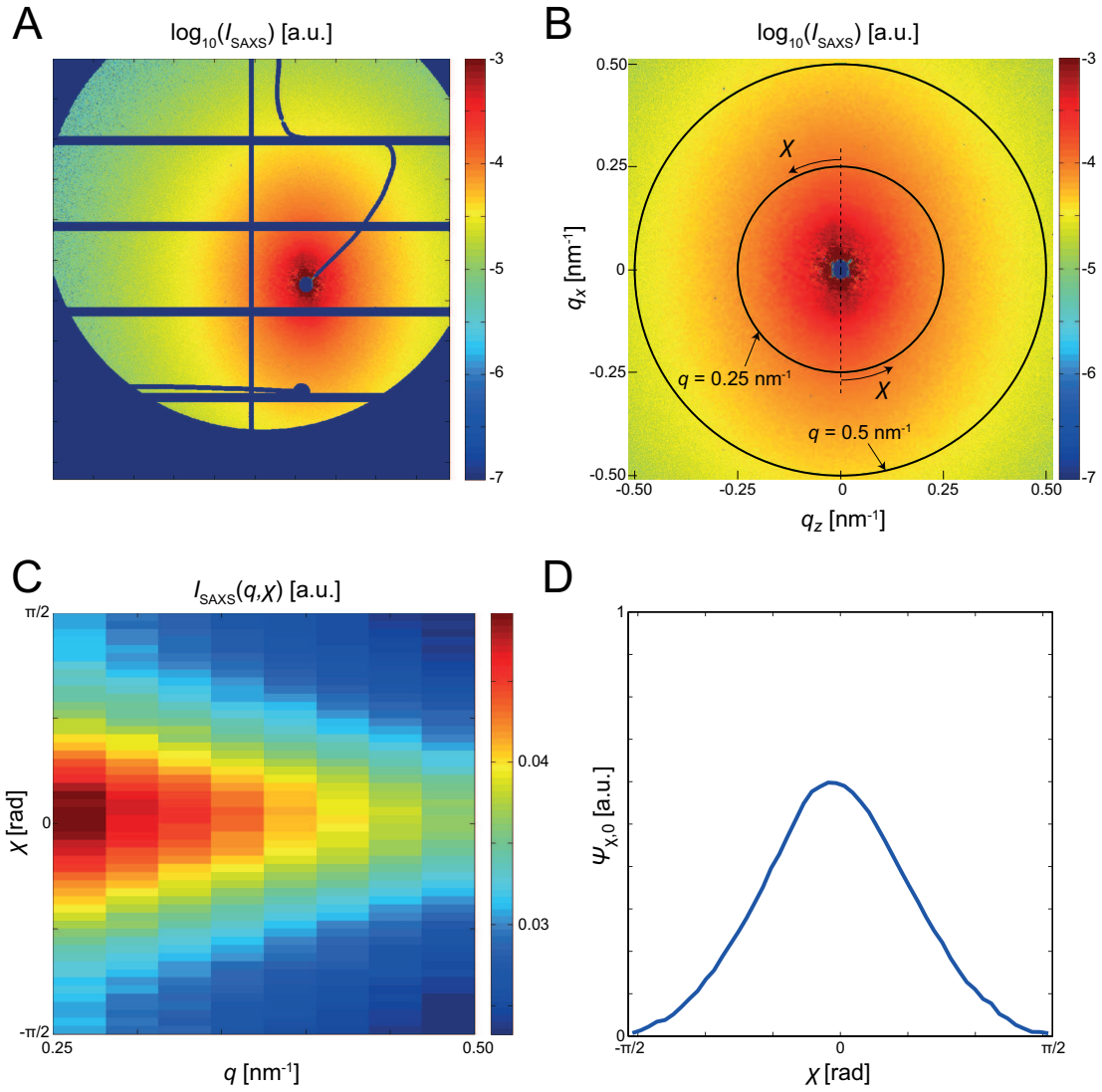
Figure 9: Example of results of the SAXS experiment at $z = 2h$ in the flow-focusing setup; (a) original scattering image; (b) mirror corrected image; (c) histogram of scattering intensity $I_{\text{SAXS}}(q, \chi)$; (d) probability distribution $\Psi_{\chi,0}$.
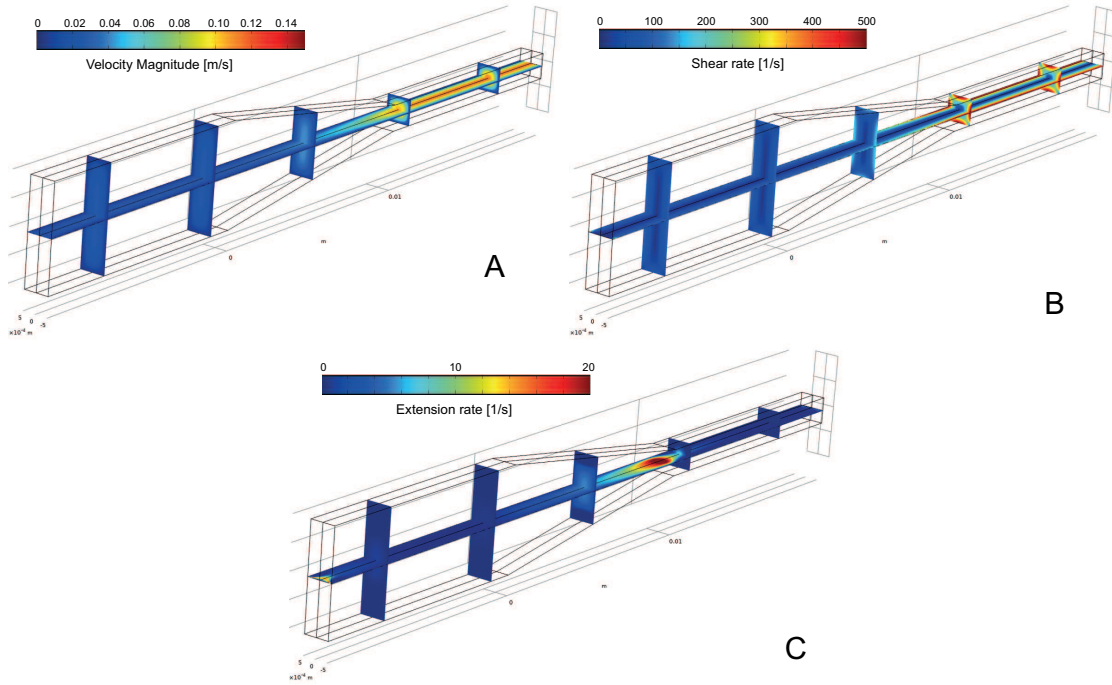
Figure 10: Illustration of the Comsol simulations at $Q_{\mathrm{ref}} = 200$ ml/h to obtain the velocity field and gradients in the CC geometry; (a) velocity magnitude; (b) shear rate $\dot{\gamma}$; (c) extension rate strain $\dot{\varepsilon}_z$.

Obtaining velocity gradients in the CC geometry

To obtain the velocity field in the CC geometry, computational fluid dynamics (CFD) simulations were performed in Comsol Multiphysics v5.5. A fully laminar flow was simulated at $Q_{\mathrm{ref}} = 200$ ml/h of a Newtonian fluid with viscosity and density of water at room temperature. The resulting velocity field $\boldsymbol{u} = (u, v, w)$ is illustrated in Fig. 10a.

Definition of strain, extension and shear rates

From the velocity field, the local velocity gradient matrix $\mathbb{J}$ can be extracted:

$$
\mathbb{J} = \begin{pmatrix} \dfrac{\partial u}{\partial x} & \dfrac{\partial u}{\partial y} & \dfrac{\partial u}{\partial z} \\[2mm] \dfrac{\partial v}{\partial x} & \dfrac{\partial v}{\partial y} & \dfrac{\partial v}{\partial z} \\[2mm] \dfrac{\partial w}{\partial x} & \dfrac{\partial w}{\partial y} & \dfrac{\partial w}{\partial z} \end{pmatrix}.
\tag{13}
$$

18

The strain rate tensor $\mathbb{E}$ is given by the symmetric part of $\mathbb{J}$, according to $\mathbb{E} = (\mathbb{J} + \mathbb{J}^{\mathrm{T}})/2$. The strain rate $\dot{\varepsilon}$ is further defined as the maximum absolute eigenvalue of matrix $\mathbb{E}$. Since we mainly have flow in the z-direction in the regions of interest in both the FFC and CC geometries, we define the shear rate as:

$$\dot{\gamma} = \sqrt{\left(\frac{\partial w}{\partial x}\right)^2 + \left(\frac{\partial w}{\partial y}\right)^2}, \tag{14}$$

and *extension rate* as:

$$\dot{\varepsilon}_z = \frac{\partial w}{\partial z}. \tag{15}$$

The values of extension rate $\dot{\varepsilon}_z$ and shear rate $\dot{\gamma}$ in the CC channel are illustrated in Figs. 10b-c. For the data in the main manuscript, the values of $\dot{\varepsilon}$, $\dot{\varepsilon}_z$ and $\dot{\gamma}$ are found by averaging the values inside the sub-volume defined by the regions in Fig. 4c. Worth noting, is that the shear rates are typically an order of magnitude higher than the extension rates in the channel, i.e. the deformation due to shear is much more substantial than the deformation due to extension. Due to the nature of the laminar flow, all velocities at a certain flow rate Q can be found by scaling with the factor Q/Q_{ref}.

Rotary diffusion of dilute stiff rods

The rotary diffusion coefficient of dilute, monodispersed slender prolate spheroids with length L and aspect ratio $r_p > 10$ (major axis divided by minor axis) is given by the expression:[12]

$$D_r = \underbrace{\frac{3[2\ln(2r_p) - 1]}{2\pi}}_{C} \frac{k_B T}{\mu L^3}, \tag{16}$$
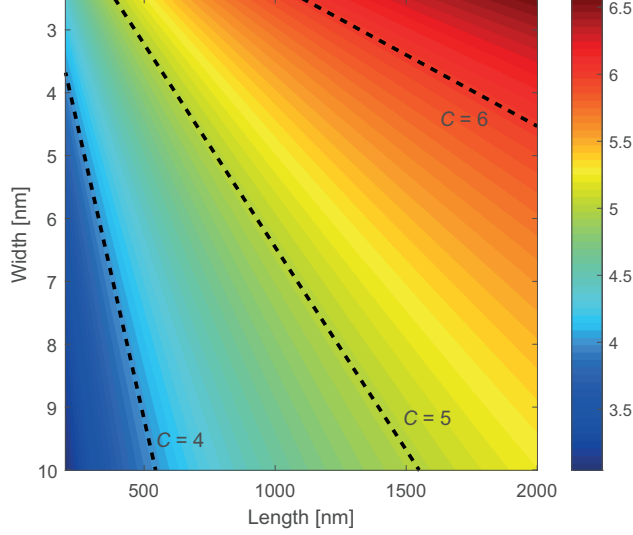
Figure 11: The prefactor C in Eq. 16 as function of particle length and particle width; the dashed lines indicate the values of $C = 4$ ($r_p = 54.4$), $C = 5$ ($r_p = 154.9$) and $C = 6$ ($r_p = 441.4$).

where μ is the dynamic viscosity of the solvent, k_B is the Boltzmann constant and T is the temperature. For large aspect ratios $r_p \gg 10$, the rotary diffusion is only very weakly dependent on r_p and thus also the particle width. The cellulose nanofibrils have widths in the range of 2.5-10 nm, and lengths usually in the span of 200-2000 nm. How the prefactor C in the expression varies with repsect to length and width is illustrated in Fig. 11 and within our experimental range, the value of C typically varies between 4 and 6. To have an expression of the *apparent hydrodynamic length* not dependent on particle width in this study, we choose the prefactor $C = 5$. The definition of the apparent hydrodynamic length L thus becomes:

$$L = \sqrt[3]{\frac{5k_B T}{\mu D_r}}, \tag{17}$$

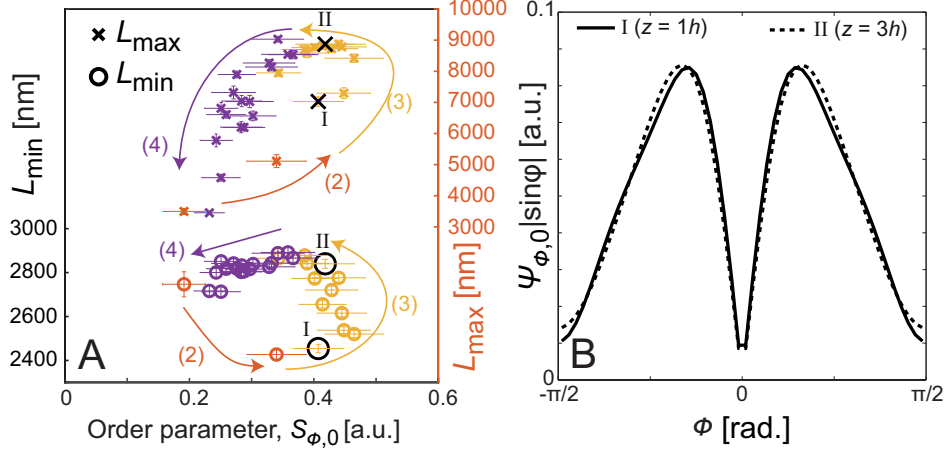where in this study we use $\mu = 10^{-3}$ Pa s and $T = 293$ K.

Figure 12: Analysis of apparent lengths of fibrils compared with orientation in the FFC geometry ($Q_1 = 23.4$ ml/h, $Q_2 = 27.0$ ml/h): (a) L_{min} and L_{max} with respect to the steady state order parameter $S_{\phi,0}$; the bigger black symbols indicate the data at position $z = h$ and $z = 3h$, with approximately the same alignment; the regions (1)-(4) refer to the regions described in Fig. 4 in the main manuscript; (b) reconstructed steady state ODF $\Psi_{\phi,0}$ at positions $z = h$ and $z = 3h$; the ODF is multiplied with $|\sin\phi|$ to illustrate the true probability density on the unit sphere.

Detailed analysis in FFC geometry

Apparent fibril lengths versus orientation distributions

It has been previously hypothesized[3] that the rotary diffusion process of CNF could be modeled using only the instantaneous orientation distribution. If this would be the case, then it means that it is likely that the same order parameter $S_{\phi,0}$ would yield the same values of L_{min} and L_{max}. These apparent lenghts are plotted versus the order parameter $S_{\phi,0}$ in Fig. 12a, results in a clear hysteresis, where the same order parameter $S_{\phi,0}$ can yield two different rotary diffusion timescales depending on if the measurement is upstream or downstream of the focusing region. For example at $z = h$ and $z = 3h$ the order parameters are close to $S_{\phi,0} = 0.4$ for both positions. However, even though the alignment is almost the same at the two positions, there is a big difference in rotary diffusion timescales. At position $z = h$, we find $L_{min} = 2454$ nm and $L_{max} = 7028$ nm, while at position $z = 3h$, we find $L_{min} = 2840$ nm and $L_{max} = 8871$ nm. Since the order parameter $S_{\phi,0}$ still only

21

is an integrated value of the actual orientation distribution function (ODF), the difference could possibly be accredited to a difference in the ODFs at the two positions. To verify this assumption, the two steady state ODFs $\Psi_{\phi,0}$ obtained from the SAXS experiments at these positions are illustrated in Fig. 12b, based on which it is inferred that the ODFs are more or less the same for a given order parameter $S_{\phi,0}$ regardless whether the alignment is increased due to the acceleration or decreased due to rotary diffusion. Thus, the difference in timescales between $z = h$ and $z = 3h$ can not be related to differences in the ODF. The main conclusion is that the alignment at $z = h$ is mainly determined by short fibrils, while the alignment at $z = 3h$ is mainly determined by longer (at least partially entangled) fibrils. Interestingly, even though different fibrils contribute to the alignment at the two positions, the ODF reconstructed from SAXS data remains almost the same (Fig. 12b), and thus X-rays are unable to capture the entire nanoscale dynamics that is obtained with the POM measurements.

References

(1) Mittal, N.; Jansson, R.; Widhe, M.; Benselfelt, T.; Håkansson, K. M.; Lundell, F.; Hedhammar, M.; Söderberg, L. D. Ultrastrong and Bioactive Nanostructured Bio-Based Composites. *ACS Nano* **2017**, *11*, 5148–5159.

(2) Cubaud, T.; Notaro, S. Regimes of Miscible Fluid Thread Formation in Microfluidic Focusing Sections. *Phys. Fluids* **2014**, *26*, 122005.

(3) Håkansson, K. M. O.; Lundell, F.; Prahl-Wittberg, L.; Söderberg, L. D. Nanofibril Alignment in Flow Focusing: Measurements and Calculations. *J. Phys. Chem. B* **2016**, *120*, 6674–6686.

(4) Rosén, T.; Brouzet, C.; Roth, S. V.; Lundell, F.; Söderberg, L. D. Three-Dimensional

Orientation of Nanofibrils in Axially Symmetric Systems Using Small-Angle X-ray Scattering. *J. Chem. Phys. C* **2018**, *122*, 6889–6899.

(5) Jeffery, G. B. The Motion of Ellipsoidal Particles Immersed in a Viscous Fluid. *Proc. R. Soc. Lond. A* **1922**, *102*, 161–179.

(6) Brouzet, C.; Mittal, N.; Lundell, F.; Söderberg, L. D. Characterizing the Orientational and Network Dynamics of Polydisperse Nanofibres at the Nanoscale. *Macromolecules* **2018**, *52*, 2286–2295.

(7) Van Gurp, M. The Use of Rotation Matrices in the Mathematical Description of Molecular Orientations in Polymers. *Colloid Polym. Sci.* **1995**, *273*, 607–625.

(8) Lim, K.; Kapitulnik, A.; Zacher, R.; Heeger, A. Conformation of Polydiacetylene Macromolecules in Solution: Field Induced Birefringence and Rotational Diffusion Constant. *J. Chem. Phys.* **1985**, *82*, 516.

(9) Rosenblatt, C.; Frankel, R. B.; Blakemore, R. P. A Birefringence Relaxation Determination of Rotational Diffusion of Magnetotactic Bacteria. *Biophys. J.* **1985**, *47*, 323–325.

(10) Håkansson, K. M.; Fall, A. B.; Lundell, F.; Yu, S.; Krywka, C.; Roth, S. V.; Santoro, G.; Kvick, M.; Wittberg, L. P.; Wågberg, L. et al. Hydrodynamic Alignment and Assembly of Nanofibrils Resulting in Strong Cellulose Filaments. *Nat. Commun.* **2014**, *5*, 4018.

(11) Stribeck, N. *X-Ray Scattering of Soft Matter*; Springer Science & Business Media, Berlin Heidelberg, 2007.

(12) Doi, M.; Edwards, S. F. *The Theory of Polymer Dynamics*; Oxford university press, New York, 1986.